

Hierarchical off-diagonal low-rank approximation of Hessians in inverse problems, with application to ice sheet model initialization

Tucker Hartland¹, Georg Stadler², Mauro Perego³, Kim Liegeois³, Noémi Petra¹

¹ Department of Applied Mathematics, University of California, Merced

E-mail: thartland@ucmerced.edu

² Courant Institute of Mathematical Sciences, New York University

³ Center for Computing Research, Sandia National Laboratories

Abstract. Obtaining lightweight and accurate approximations of Hessian applies in inverse problems governed by partial differential equations (PDEs) is an essential task to make both deterministic and Bayesian statistical large-scale inverse problems computationally tractable. The $\mathcal{O}(N^3)$ computational complexity of dense linear algebraic routines such as that needed for sampling from Gaussian proposal distributions and Newton solves by direct linear methods, can be reduced to log-linear complexity by utilizing hierarchical off-diagonal low-rank (HODLR) matrix approximations. In this work, we show that a class of Hessians that arise from inverse problems governed by PDEs are well approximated by the HODLR matrix format. In particular, we study inverse problems governed by PDEs that model the instantaneous viscous flow of ice sheets. In these problems, we seek a spatially distributed basal sliding parameter field such that the flow predicted by the ice sheet model is consistent with ice sheet surface velocity observations. We demonstrate the use of HODLR approximation by efficiently generating Hessian approximations that allow fast generation of samples from a Gaussianized posterior proposal distribution. Computational studies are performed which illustrate ice sheet problem regimes for which the Gauss-Newton data-misfit Hessian is more efficiently approximated by the HODLR matrix format than the low-rank (LR) format. We then demonstrate that HODLR approximations can be favorable, when compared to global low-rank approximations, for large-scale problems by studying the data-misfit Hessian associated to inverse problems governed by the Stokes flow model on the Humboldt glacier and Greenland ice sheets.

1. Introduction

Model-based simulation of complex physical systems plays an essential role in understanding real world phenomena. These models are often characterized by partial differential equations (PDEs), and are typically subject to uncertainties stemming from unknown coefficient fields, constitutive laws, source terms, initial and/or boundary conditions, geometries, etc. When observation data exist, these parameters can be estimated by solving an inverse problem governed by the underlying model (e.g., PDE). It is well known that uncertainty is a fundamental feature of inverse problems, therefore in addition to inferring the parameters of interest, we need to quantify the uncertainty associated with this inference. This uncertainty quantification can be done via Bayesian inference. Solving Bayesian inverse problems governed by complex PDEs can be extremely challenging due to high-dimensional parameter spaces that stem from discretization of infinite-dimensional parameter fields and the need to repeatedly solve the underlying PDEs. To overcome these computational challenges, it is essential to exploit problem structure, when possible. For example, the underlying PDE solution operator is often diffusive, that observation data may be sparse or only contain limited information about the parameter field. These particularities give rise to a low-rank structure in the second derivative of the data-misfit component of the inverse problem objective (or of the negative log likelihood), hereafter referred to as the data-misfit Hessian. In previous work [1, 2] we exploited this low-rank structure in the context of inverse ice sheet flow problems. However, for cases when this “low-rank” is in fact large, as is the case for many inverse problems of practical interest, where the observation data are highly informative, low-rank approximation is insufficient. In this article, we exploit the local sensitivity of model predictions to parameters, which gives rise to an off-diagonal low-rank structure. We do so by invoking hierarchical off-diagonal low-rank (HODLR) matrix approximations and detail how they can be used to reduce the computational cost to solve large-scale PDE-based inverse problems.

Related work Global low-rank approximation of Hessians in inverse problems have been successfully utilized in [1, 3, 4, 5, 6], with deterministic and randomized methods [7, 5] being available to generate said approximations. However, some problems, specifically those with highly informative observation data, are not amenable to global low-rank approximation, and thus other structure-exploiting strategies are needed such as those based on local translation invariance and localized sensitivities [8, 9, 10]. Here we focus on hierarchical low-rank methods for which convenient randomized methods are available [11, 12].

Hierarchical matrices have been demonstrated in [13, 14] to be an effective means to approximate covariance matrices associated to large-scale Gaussian processes. In [15], hierarchical matrix approximations with general hierarchical partitioning patterns are utilized for the construction of explicit representations of Hessian inverses. In one of the examples studied, the authors find that the diffusivity of the parameter-to-PDE-solution

map and the informativeness of the observation data impact whether the data-misfit Hessian is more suited for compression with hierarchical or global low-rank formats. Here, we build on this study and focus on a specific inverse problem arising in land ice modeling.

Contributions The main contributions of this work are as follows. (1) We motivate the use of HODLR compression for data-misfit Hessians in inverse problems governed by PDEs, and present a detailed study for large-scale ice sheet inverse problems, such as the Greenland ice sheet. (2) We describe a strategy that leverages the fast manipulation of HODLR matrices to efficiently generate approximate samples from a Gaussian posterior distribution for uncertainty quantification. (3) We numerically study the influence of various problem setups on the off-diagonal low-rank structure of the data-misfit Hessian. The results show the effectiveness of the HODLR approximation for various problem scales including for a Greenland ice sheet inverse problem, which has a discretized parameter dimension of 3.2×10^5 .

2. Preliminaries

In this section, we summarize background material regarding the solution of discretizations of infinite-dimensional inverse problems. We also briefly review HODLR matrices. Specifically, we define HODLR matrices, list some of their properties and summarize the computational complexities of computing symmetric HODLR matrix approximations of symmetric operators that are only available through their application on vectors. We refer to [16, 17] for a more thorough discussion of hierarchical matrices and to [12] for more detail on HODLR matrices.

2.1. Bayesian Inverse Problems

A means to account for uncertainty in parametric inference is to employ the Bayesian approach to inverse problems [18, 19, 20], which takes as input observation data \mathbf{d} , i.e., the data, prior knowledge of the parameter and a model for the likelihood of data conditional to β . Prior knowledge of the discretized parameter β is typically determined by the expertise of domain scientists and mathematically encoded in a probability density function $\pi_{\text{prior}}(\beta)$. The likelihood $\pi(\mathbf{d}|\beta)$ involves the data uncertainty and the mathematical model for the parameter-to-observable process. The solution of a Bayesian inverse problem is a probability density function for the discretized parameter β , that is conditioned on the observation data according to Bayes formula

$$\pi_{\text{post}}(\beta) = \pi(\beta|\mathbf{d}) \propto \pi_{\text{prior}}(\beta) \pi(\mathbf{d}|\beta),$$

which provides a formal expression for the posterior distribution. Here, “ \propto ” means equal up to a normalization constant. For a problem with Gaussian prior $\mathcal{N}(\bar{\beta}, \mathbf{\Gamma}_{\text{prior}})$

and data noise $\boldsymbol{\eta}$ described by the zero mean Gaussian $\mathcal{N}(\mathbf{0}, \boldsymbol{\Gamma}_{\text{noise}})$, $\pi_{\text{post}}(\cdot)$ has the following form

$$\pi_{\text{post}}(\boldsymbol{\beta}) \propto \exp\left(-\frac{1}{2}\|\mathcal{F}(\boldsymbol{\beta}) - \mathbf{d}\|_{\boldsymbol{\Gamma}_{\text{noise}}^{-1}}^2 - \frac{1}{2}\|\boldsymbol{\beta} - \bar{\boldsymbol{\beta}}\|_{\boldsymbol{\Gamma}_{\text{prior}}^{-1}}^2\right), \quad (1)$$

where \mathcal{F} is the parameter-to-observable map. The notation $\|\cdot\|_{\mathbf{A}}$ means that the norm is weighted with the positive-definite matrix \mathbf{A} , i.e., $\|\mathbf{v}\|_{\mathbf{A}} = \sqrt{\mathbf{v}^\top \mathbf{A} \mathbf{v}}$. The parameter-to-PDE-solution map is typically nonlinear, and consequently the posterior distribution is not a Gaussian. One characteristic of the posterior distribution is the point at which it is maximized, or equivalently the point which minimizes the negative log-posterior, the so-called maximum a posteriori (MAP) point,

$$\boldsymbol{\beta}^* := \arg \min_{\boldsymbol{\beta}} J(\boldsymbol{\beta}) := \frac{1}{2}\|\mathcal{F}(\boldsymbol{\beta}) - \mathbf{d}\|_{\boldsymbol{\Gamma}_{\text{noise}}^{-1}}^2 + \frac{1}{2}\|\boldsymbol{\beta} - \bar{\boldsymbol{\beta}}\|_{\boldsymbol{\Gamma}_{\text{prior}}^{-1}}^2. \quad (2)$$

A means to compute the MAP point is to employ a (Gauss) Newton method for optimization [21], which critically relies on the availability of the (Gauss-Newton) Hessian. Since, J is defined implicitly in terms of the parameter-to-observable map, which involves a PDE solution operator, we utilize the adjoint method [22, 23, 24] to compute its gradient and Hessian-applies.

To fully explore posterior distributions, Markov chain Monte-Carlo (MCMC) techniques [25, 26] can be used. Such techniques require a proposal distribution that ideally approximates the posterior and is easily sampled from. One method to generate a Gaussian proposal distribution is through the Laplace approximation of the posterior about $\boldsymbol{\beta}_k$ (or around the MAP point)

$$\tilde{\pi}_{\text{post}}(\boldsymbol{\beta}, \boldsymbol{\beta}_k) \propto \exp\left(-\frac{1}{2}\langle \boldsymbol{\beta} - \boldsymbol{\mu}_k, \mathbf{H}_k(\boldsymbol{\beta} - \boldsymbol{\mu}_k) \rangle_{\ell^2}\right), \boldsymbol{\mu}_k = \boldsymbol{\beta}_k - \mathbf{H}_k^{-1} \mathbf{g}_k,$$

where \mathbf{g}_k , \mathbf{H}_k are the gradient and Hessian of the log-posterior $J(\boldsymbol{\beta})$ at $\boldsymbol{\beta}_k$. Another MCMC sampling approach is the generalized preconditioned Crank-Nicholson (gpCN) method [27, 28]. An attractive choice for the preconditioner is the Hessian at the MAP point, [29].

For these and other MCMC samplers, one typically needs to apply the inverse Hessian \mathbf{H}_k^{-1} or its square root $\mathbf{H}_k^{-1/2}$ repeatedly and efficiently, which also motivates the study presented in this paper. In particular, in Section 3.2 we discuss how HODLR approximations can be used for the fast application of the Hessian square root.

2.2. Symmetric HODLR Matrices

A HODLR matrix $\mathbf{A} \in \mathbb{R}^{N \times N}$, is a matrix equipped with a depth $L \in \mathbb{N}$, hierarchical partitionings of the index set $\mathcal{I} = \{1, 2, \dots, N\}$ into contiguous subsets and low-rank off-diagonal blocks defined by the partition, which is described in greater detail in e.g. [12]. The block rank-structure of a HODLR matrix for various hierarchical depths is illustrated in Figure 1. An HODLR matrix must satisfy two additional properties.

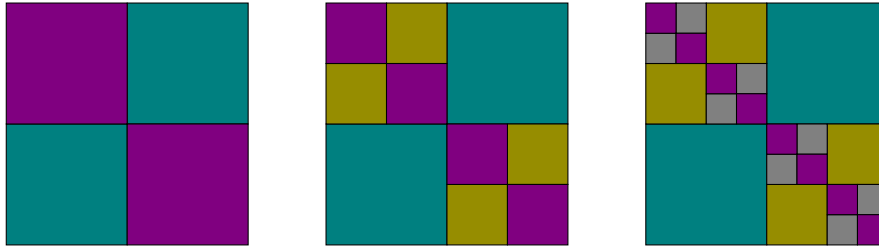


Figure 1: Rank-structure of a matrix \mathbf{A} with hierarchical depths $L = 1$ (left), $L = 2$ (middle) and $L = 3$ (right). Off-diagonal blocks are assumed to be low-rank.

- (i) The depth of the hierarchical partitioning scales with the logarithm of the size of the matrix, i.e.,

$$L = \mathcal{O}(\log N).$$

- (ii) The maximum rank of each hierarchical level ℓ off-diagonal block, r_ℓ , is bounded above by a number r that is independent of the problem size N , for each level ℓ

$$\max_{1 \leq \ell \leq L} r_\ell \leq r = \mathcal{O}(1).$$

Such matrices are referred to as data-sparse since the low-rank blocks allow for them to be represented computationally with less than $\mathcal{O}(N^2)$ floating point numbers. In particular, the storage of an HODLR matrix is $\mathcal{O}(N \log N)$, $\mathcal{O}(N \log N)$ flops are needed to compute a HODLR matrix-vector product [7], and $\mathcal{O}(N \log^2 N)$ flops are required for direct methods to compute an inverse HODLR matrix-vector product [30], as well as square root and inverse square root matrix-vector products [31].

Compression We aim to generate HODLR approximations of data-misfit Hessians in inverse problems. For large-scale problems, the data-misfit Hessian is available only as a matrix-free operator. In order to construct HODLR approximations of symmetric matrix-free operators, we employ previously developed randomized linear algebraic routines which only require the matrix-free action on a limited number of random vectors with specified null entries, referred to as *structured* random vectors. The Hessian action on these structured random vectors is used to sample row and column spaces of off-diagonal Hessian submatrices and allow for randomized approximate truncated singular value decompositions of the aforementioned off-diagonal submatrices. More details can be found in the appendix, see Algorithm 2.

For the results that we present in Section 5 a rank-adaptive symmetric matrix-free [32, 33], hierarchical compression algorithm is utilized, that is based on [12]. A similar algorithm is presented in [34], wherein the hierarchical partitioning is more general and the low-rank blocks have nested bases. The rank-adaptivity provides a high probability means of resolving the off-diagonal blocks to a desired level of accuracy. By utilizing available matrix-vector product information and the Rayleigh quotient, a rank adaptive relative tolerance algorithm is made possible.

Computational Cost of Generating HODLR Approximations The number of matrix-vector products ζ , needed to compress a symmetric matrix using d oversampling vectors, into a level L HODLR matrix with off-diagonal ranks $\{r_\ell\}_{\ell=1}^L$ is given by

$$\zeta = 2(\langle r \rangle + d)L + N/2^L, \text{ where } \langle r \rangle := \frac{1}{L} \sum_{\ell=1}^L r_\ell. \quad (3)$$

Equation 3 can be understood from Algorithm 2 in Appendix 8.1, as for each level ℓ one needs to compute $r_\ell + d$ Hessian vector products, in order to compute \mathbf{Y} (line 7 of Algorithm 2) and $r_\ell + d$ Hessian vector products to compute \mathbf{Z} (line 14 of Algorithm 2). The remaining $N/2^L$ Hessian vector products arise from the need to determine the diagonal subblocks, which is detailed in [7]. We note that with an adaptive procedure to determine an approximate basis \mathbf{Q} , such as that in [33], for a block matrix column space, the cost is reduced to $\zeta_{\text{adaptive}} = 2(\langle r \rangle + d/2)L + N/2^L$ but with the additional computational burden of extra orthogonalization routine calls. We note that $\zeta = \mathcal{O}(\log N)$ matrix-vector products are needed to generate an HODLR approximation of a matrix with HODLR structure. For sufficiently large problems HODLR compression is not expected to be more computationally efficient than global low-rank (LR) compression, as $\zeta^{\text{LR}} = r + d$, the number of matrix-vector products to generate a rank r compression by the single-pass algorithm [12] with d oversampling vectors is independent of the problems size. However, for problems of substantial size, we observe that the HODLR format does offer computational savings (see Section 6).

3. HODLR matrices in inverse problems governed by PDEs

Here, we illustrate why data-misfit Hessians in inverse problems governed by PDEs may contain numerically low-rank off-diagonal blocks, describe how one can permute parameters to expose this HODLR structure, and show how HODLR approximations can be leveraged to draw samples from Gaussian approximations of Bayesian posterior distributions.

3.1. Motivation

Consider the following data-misfit cost functional

$$J_{\text{misfit}}(\beta) := \frac{1}{2} \|\mathcal{F}(\beta) - \mathbf{d}\|_{\mathbf{\Gamma}_{\text{noise}}^{-1}}^2, \quad \text{with } \mathcal{F}(\beta) = \mathbf{B}u,$$

where \mathbf{B} linearly maps the PDE solution $u = u(\beta)$, for the spatially-distributed parameter field β , to the model predictions associated to the data \mathbf{d} . Moreover, $\mathbf{\Gamma}_{\text{noise}}$ is the covariance matrix describing the Gaussian noise of the observational data. For illustration purposes, we assume that the parameter function β is defined on a region Γ_1 and the data \mathbf{d} is observed on a region Γ_2 , which may or may not be distinct. These quantities are related through the solution of the governing PDE and the measurement operator \mathbf{B} . The characteristics of this relation depends on properties of the governing PDE. In the following, we assume that a spatially (or temporally) localized perturbation

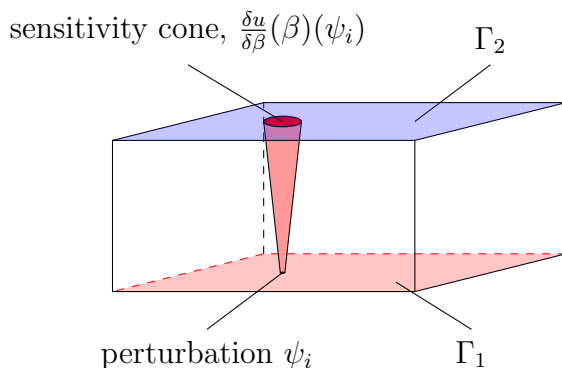


Figure 2: Sketch illustrating a case where the influence of changes in the parameter β on the PDE solution u in Γ_2 is focused in a small area. To illustrate this, we show a sensitivity cone, i.e., the PDE solution u is predominantly impacted in a cone about the support of the localized parameter perturbation.

in the β field leads to a predominantly localized effect in the PDE solution u , and thus the model predictions $\mathcal{B}u$. This property is illustrated in Figure 2, where we use a sensitivity cone to illustrate the influence of a local perturbation in β , defined over Γ_1 , on the PDE solution u in Γ_2 . It is well known that for an elliptic PDE, local perturbations influence the solution globally, but depending on the geometry of the domain and the equation, this global effect may rapidly decay outside a subset of Γ_2 that captures the main effects of the perturbation. For instance, in a problem as in Figure 2, the influence of perturbations in β on u is likely to become more localized when the distance between Γ_1 and Γ_2 decreases.

We next discuss the relationship between properties of the PDE as discussed above and off-diagonal blocks in the Hessian matrix (or its Gauss-Newton variant). The data-misfit Hessian, i.e., the Hessian of the data-misfit part of the cost functional, can be derived using the adjoint method [22, 23, 24]. However, we find that the HODLR structure of the data-misfit Hessian is most easily seen by studying a formal expression of it in terms of the first and second order sensitivities $\delta u/\delta\beta$, $\delta^2 u/\delta\beta^2$

$$\begin{aligned} \frac{\delta^2}{\delta\beta^2} J_{\text{misfit}}(\beta)(\beta_1, \beta_2) &= (\mathcal{B}u - \mathbf{d})^\top \Gamma_{\text{noise}}^{-1} \left(\mathcal{B} \frac{\delta^2 u}{\delta\beta^2}(\beta)(\beta_1, \beta_2) \right) + \\ &\quad \left(\mathcal{B} \frac{\delta u}{\delta\beta}(\beta)(\beta_1) \right)^\top \Gamma_{\text{noise}}^{-1} \left(\mathcal{B} \frac{\delta u}{\delta\beta}(\beta)(\beta_2) \right), \end{aligned}$$

where $\delta u/\delta\beta(\beta)(\beta_1)$ is the first variation [35] of u with respect to β in direction β_1 , and $\delta^2 u/\delta\beta^2(\beta)(\beta_1, \beta_2)$ is the second variation of u with respect to β in directions β_1, β_2 , that is,

$$\begin{aligned} \frac{\delta u}{\delta\beta}(\beta)(\beta_1) &:= \left[\frac{d}{d\epsilon} u(\beta + \epsilon\beta_1) \right]_{\epsilon=0}, \\ \frac{\delta^2 u}{\delta\beta^2}(\beta)(\beta_1, \beta_2) &:= \left[\frac{d}{d\epsilon} \frac{\delta u}{\delta\beta}(\beta + \epsilon\beta_2)(\beta_1) \right]_{\epsilon=0}. \end{aligned}$$

Upon discretizing β with finite elements we obtain the following formal expression for the (i, j) -entry of the data-misfit Hessian $\mathbf{H}_{\text{misfit}}$ and of the Gauss-Newton data-misfit Hessian $\mathbf{H}_{\text{misfit}}^{\text{GN}}$

$$(\mathbf{H}_{\text{misfit}})_{i,j} = \frac{\delta^2}{\delta\beta^2} \left(J_{\text{misfit}}(\beta) \right) (\psi_i, \psi_j), \quad (4)$$

$$(\mathbf{H}_{\text{misfit}}^{\text{GN}})_{i,j} = \left(\mathbf{B} \frac{\delta u}{\delta\beta}(\beta)(\psi_i) \right)^\top \mathbf{\Gamma}_{\text{noise}}^{-1} \left(\mathbf{B} \frac{\delta u}{\delta\beta}(\beta)(\psi_j) \right), \quad (5)$$

where $\{\psi_j\}_{j=1}^N$ is a basis for the nodal finite-element space, which is used to approximate β .

When sensitivities are predominantly local as discussed above and when the support of two finite element basis functions ψ_i, ψ_j are well separated, the terms

$$\left(\mathbf{B} \frac{\delta u}{\delta\beta}(\beta)(\psi_i) \right)^\top \mathbf{\Gamma}_{\text{noise}}^{-1} \left(\mathbf{B} \frac{\delta u}{\delta\beta}(\beta)(\psi_j) \right) \quad \text{and} \quad \mathbf{B} \left(\frac{\delta^2 u}{\delta\beta^2}(\beta)(\psi_i, \psi_j) \right),$$

are rather small (assuming diagonally dominant noise covariance matrices). This is, e.g., due to $\mathbf{B} \delta u / \delta\beta(\beta)(\psi_i)$ having small values when $\mathbf{B} \delta u / \delta\beta(\beta)(\psi_j)$ is large. Now, let \mathcal{I}, \mathcal{J} be disjoint index subsets of $\{1, 2, \dots, N\}$, then the entries in the matrix block $\{(\mathbf{H}_{\text{misfit}})_{i \in \mathcal{I}, j \in \mathcal{J}}\}$ of the data-misfit Hessian are relatively small whenever $\cup_{i \in \mathcal{I}} \text{supp}(\psi_i)$ and $\cup_{j \in \mathcal{J}} \text{supp}(\psi_j)$ are well separated. Such Hessian blocks are well suited for approximation by low-rank matrices. When the degrees of freedom corresponding to the finite element basis functions ψ_i are ordered such that \mathcal{I}, \mathcal{J} are contiguous, $(\mathbf{H}_{\text{misfit}})_{\mathcal{I}, \mathcal{J}}$ is an off-diagonal subblock of $\mathbf{H}_{\text{misfit}}$ and $\mathbf{H}_{\text{misfit}}$ tends to have HODLR structure as defined in Section 2.2. The Gauss-Newton data-misfit Hessian may have HODLR structure for the same reasons. In both cases, the order of the basis functions and thus the degrees of freedom influence this structure. Ideally, one wants an order that maintains locality, i.e., consecutive indices correspond to basis functions that are close to each other, and as a consequence, basis function with significantly different indices are far from each other such that the corresponding off-diagonal blocks have small entries and can be well approximated using a low-rank matrix approximation. We defer to Section 6.2 for a discussion of methods and numerical experiments regarding the order of the degrees of freedom.

3.2. Application of HODLR structure for fast sampling of Gaussian posterior approximations

In [2], the following expressions of the Gaussianized posterior covariance are provided,

$$\begin{aligned} \mathbf{\Gamma}_{\text{post}} &= (\mathbf{H}_{\text{misfit}} + \mathbf{\Gamma}_{\text{prior}}^{-1})^{-1} = \mathbf{\Gamma}_{\text{prior}}^{1/2} (\mathbf{H}'_{\text{misfit}} + \mathbf{I})^{-1} \mathbf{\Gamma}_{\text{prior}}^{\top/2}, \\ \mathbf{H}'_{\text{misfit}} &:= \mathbf{\Gamma}_{\text{prior}}^{\top/2} \mathbf{H}_{\text{misfit}} \mathbf{\Gamma}_{\text{prior}}^{1/2}, \\ \mathbf{\Gamma}_{\text{post}}^{1/2} &= \mathbf{\Gamma}_{\text{prior}}^{1/2} (\mathbf{H}'_{\text{misfit}} + \mathbf{I})^{-1/2}, \end{aligned}$$

where the matrix square-root $\mathbf{A}^{1/2}$ is such that $\mathbf{A} = \mathbf{A}^{1/2} (\mathbf{A}^{1/2})^\top$. For Bayesian inverse problems with a parameter field that is distributed spatially over a bounded subset of

\mathbb{R}^m , $m = 2, 3$, a reasonable choice is to use the square of an inverse elliptic PDE operator for the prior covariance [20], which permits a means of obtaining a symmetric square root of $\mathbf{\Gamma}_{\text{prior}}$. In previous works such as [1, 3, 4, 5, 6], the prior-preconditioned data-misfit Hessian $\mathbf{H}'_{\text{misfit}}$, was approximated by global low-rank compression. This strategy provides an efficient means of approximating the posterior covariance matrix in inverse problems with data sets that contain sufficiently small amounts of information. Here we propose to exploit HODLR problem structure and generate approximate posterior covariance matrices by HODLR approximations of the prior-preconditioned data-misfit $\tilde{\mathbf{H}}'_{\text{misfit}}$, see Appendix 8.3 for an analysis on how such an approximation impacts the accuracy of the approximate posterior covariance

$$\tilde{\mathbf{\Gamma}}_{\text{post}} = \mathbf{\Gamma}_{\text{prior}}^{1/2} \left(\tilde{\mathbf{H}}'_{\text{misfit}} + \mathbf{I} \right)^{-1} \mathbf{\Gamma}_{\text{prior}}^{\top/2}.$$

A symmetric square-root factorization of $\tilde{\mathbf{H}}'_{\text{misfit}} + \mathbf{I}$ is then generated with $\mathcal{O}(N \log^2 N)$ flops [31]. The symmetric factorization allows for a $\mathcal{O}(N \log N)$ means of applying both the square root and inverse square root.

4. Bayesian inverse ice sheet problems

The simulation of the dynamics of ice sheets (e.g., the Greenland or Antarctic ice sheets) is an important component of coupled climate simulations. Such simulations require estimation of a present state of the ice that is consistent with available observations, a process sometimes referred to as model initialization. This estimation problem can be formulated either as a deterministic inverse problem (i.e., as nonlinear least squares optimization governed by PDEs) or as a Bayesian inverse problem (i.e., as a statistical problem which aims to characterize a distribution of states). The latter approach, while more expensive, provides uncertainty estimates in addition to determining a best parameter fit.

Ice sheet dynamics [36] is typically governed by nonlinear Stokes equations or simplifications thereof, such as the first-order equations (see e.g., [37]). Generally, the most uncertain component in ice sheet simulations is the basal boundary condition, i.e., how the ice sheet interacts with the rock, sand, water or a mix thereof at its base. Estimating an ice sheet's effective boundary condition from velocity observations on the top surface, the ice sheet's geometry and a model for its dynamics is thus an important problem that can mathematically formulated as an inverse problem [1, 38, 39, 40, 41].

We summarize the formulation of this inverse problem next. As common in the literature, we use a *snapshot* optimization approach, where all the data are assumed to be collected over a short period of time during which changes in the ice geometry are negligible. We denote the bounded domain covered by ice by $\Omega \subset \mathbb{R}^m$, $m \in \{2, 3\}$, and the basal, lateral and top parts of the domain boundary $\partial\Omega$ by Γ_b , Γ_l , and Γ_t , as illustrated in Figure 3.

The governing equations are nonlinear incompressible Stokes equations whose solution is the ice flow velocity $\mathbf{u} : \Omega \rightarrow \mathbb{R}^m$ and the pressure $p : \Omega \rightarrow \mathbb{R}$ given as

follows:

$$-\nabla \cdot \boldsymbol{\sigma}_u = \rho \mathbf{g} \quad \text{in } \Omega, \quad (6)$$

$$\nabla \cdot \mathbf{u} = 0 \quad \text{in } \Omega, \quad (7)$$

$$\boldsymbol{\sigma}_u \mathbf{n} = \mathbf{0} \quad \text{on } \Gamma_t, \quad (8)$$

$$\mathbf{u} \cdot \mathbf{n} = 0 \text{ and } \mathbf{T}(\boldsymbol{\sigma}_u \mathbf{n} + \exp(\beta) \mathbf{u}) = \mathbf{0} \quad \text{on } \Gamma_b, \quad (9)$$

along with additional lateral boundary conditions. Here, β is a basal sliding parameter field, $\rho \mathbf{g}$ the body force density, where ρ is the mass density of the ice and \mathbf{g} the acceleration due to gravity. Equation 6 describes the conservation of momentum, 7 the conservation of mass, and 8 are stress-free boundary conditions for the top surface (the ice-air interface). In normal direction, Equation 9 states a non-penetration condition, i.e., the ice cannot flow into the rock/sand layer which supports it (here \mathbf{n} denotes the outward unit normal to the boundary $\partial\Omega$ and \mathbf{T} the tangential operator, $\mathbf{T}\mathbf{v} = \mathbf{v} - \mathbf{n}(\mathbf{n}^\top \mathbf{v})$). In tangential direction, Equation 9 specifies a tangential sliding condition that relates the fraction of tangential sliding and tangential stress through the (logarithmic) basal sliding field $\beta = \beta(x)$, $x \in \Gamma_b$. We employ Glen's flow law [42], a constitutive law for ice that relates the stress tensor $\boldsymbol{\sigma}_u$ and the strain rate tensor $\dot{\boldsymbol{\epsilon}}_u = \frac{1}{2}(\nabla \mathbf{u} + \nabla \mathbf{u}^\top)$,

$$\boldsymbol{\sigma}_u = 2\eta(\mathbf{u}) \dot{\boldsymbol{\epsilon}}_u - \mathbf{I}p, \text{ with } \eta(\mathbf{u}) = \frac{1}{2} A^{-1/n} \dot{\boldsymbol{\epsilon}}_{\text{II}}^{\frac{1-n}{2n}}, \quad (10)$$

where η is the effective viscosity, \mathbf{I} is the unit matrix, $\dot{\boldsymbol{\epsilon}}_{\text{II}} = \text{tr}(\dot{\boldsymbol{\epsilon}}_u^2)$ is the second invariant of the strain rate tensor, A is a flow rate factor, and n is Glen's exponent. Ice is typically modeled using $n \approx 3$, which corresponds to a shear-thinning constitutive relation, here we use $n = 3$.

As discussed above, the parameter containing the largest uncertainty is the (logarithmic) basal sliding field $\beta = \beta(x)$. Thus, it is usually the parameter inferred from (typically, satellite) observation data \mathbf{d} , here in the form of surface velocity measurements. Using an appropriate point observation operator \mathcal{B} that extracts point data from the solution \mathbf{u} of the governing equations 6-9, and assuming additive observation errors $\boldsymbol{\eta}$, the relationship between model and data is now of the typical form

$$\mathbf{d} = \mathcal{B}\mathbf{u} + \boldsymbol{\eta}. \quad (11)$$

Assuming that the observation errors $\boldsymbol{\eta}$ and the prior for the parameter field β follow Gaussian distributions, we are in the framework of Bayesian inverse problems summarized in Section 2.1.

5. Example I: Two-dimensional ISMIP-HOM benchmark

We first study the prospects of compressing the Gauss-Newton data-misfit Hessian in a problem inspired by the ISMIP-HOM collection of ice sheet simulation benchmark problems [43]. This problem set was used to explore inverse ice sheet problems in [40, 41]. After a short description of the problem setup, we present results such as the MAP

point estimate β^* and approximate Gaussianized posterior samples using an HODLR compression of the posterior covariance. Then, we study the impact that various problem features have on the suitability of the Gauss-Newton data-misfit Hessian for compression to the HODLR and global low-rank formats.

5.1. Problem setup

This problem setup consists of a rectangular piece of ice on a slope, as sketched in Figure 3. This simple example allows us to study the influence of the domain aspect ratio, the number of observations and the level of mesh refinement on the properties of the Gauss-Newton data-misfit Hessian matrix. The domain has a width of $W = 10^4$ [m] and a height of $H = 10^2$ [m]. Periodic boundary conditions are employed along the lateral boundaries such that the setup models an infinite slab of ice on a slope. The governing equations and other boundary conditions are as discussed in Equations 6-9.

The Stokes equations are discretized using Taylor-Hood finite elements on a mesh of 256×10 rectangles, each subdivided into two triangles, for the domain length $[0, W)$ and height $[0, H]$. To compute a MAP estimate, we generate synthetic surface velocity data using the “true” logarithmic basal sliding field, $\beta_{\text{true}}(x) := \log(1200 + 1100 \sin(\frac{2\pi x}{W}))$. Given this basal sliding field, we solve Equations 6-9, extract the tangential velocity component at 100 uniformly distributed points on the top boundary Γ_t , and add 1% relative Gaussian noise to each data point, resulting in the synthetic data \mathbf{d} .

It remains to define the prior distribution for the parameter field β . The average value of β_{true} is used as constant prior mean $\bar{\beta}(x) = 6.73315 \approx \frac{1}{W} \int_0^W \beta_{\text{true}}(s) ds$. The prior covariance matrix $\mathbf{\Gamma}_{\text{prior}}$ is a discretization of the covariance PDE operator $\mathcal{C} := (\delta I - \gamma \Delta)^{-1}$, with $\gamma = 6 \times 10^2$ and $\delta = 2.4 \times 10^{-3}$, with Robin boundary conditions [44]. These values are chosen in order to provide a relatively large prior correlation length of 10^3 [m] [45]. Next, we summarize the computation of the MAP point and the compression of the Gauss-Newton data-misfit Hessian matrix at the MAP point.

5.2. MAP point and HODLR Gaussianized posterior

The nonlinear optimization problem for finding the MAP estimate is solved using an inexact Gauss-Newton minimization method with backtracking linesearch [21], where the linear systems are iteratively solved by the conjugate gradient method. The resulting MAP point is shown in Figure 4. The MAP parameter field β^* , closely resembles the true parameter β_{true} , which is a consequence of the large amount of available data and relatively small noise level.

Next, we use the Gaussianized posterior distribution with a compressed prior-preconditioned data-misfit Hessian $\mathbf{H}'_{\text{misfit}}$ to generate approximate samples from the posterior distribution. Upon construction of the HODLR compression of the prior-preconditioned data-misfit Hessian (details and comparisons can be found below in

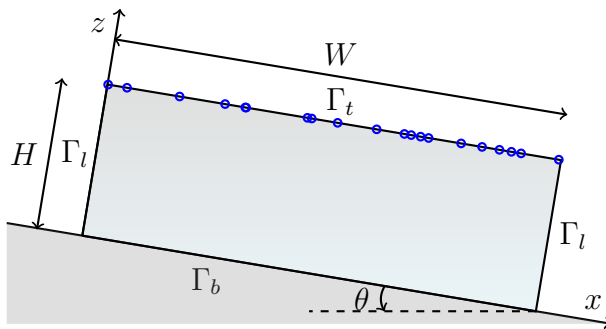


Figure 3: Schematic of two-dimensional slab of ice used for Example I in Section 5. The blue circles show representative (random) measurement locations. The angle θ is the slope of the ice slab.

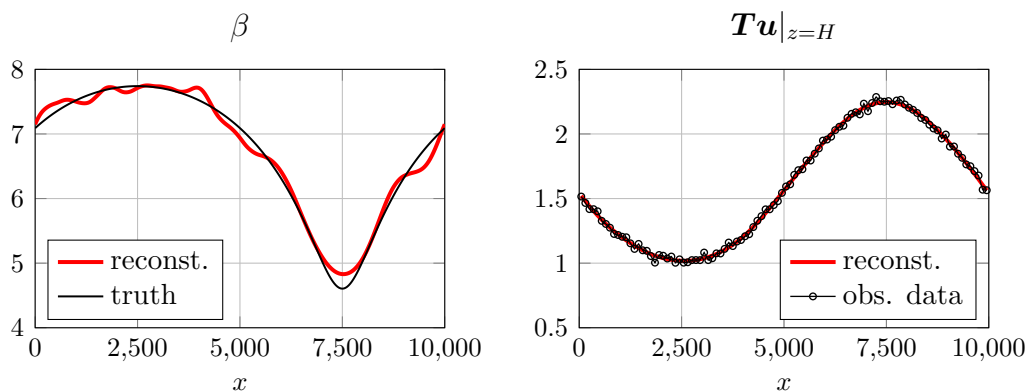


Figure 4: Shown for Example I are on the left the MAP point β^* (red) and the truth basal sliding parameter β_{true} (black) used to generate synthetic observations of the tangential velocity component on the upper surface Γ_t . Shown on the right are noisy synthetic observations (black dots) used for computing the MAP point and the associated tangential surface velocity reconstruction (red).

Section 5.3), we draw samples from the HODLR Gaussianized posterior as outlined in Section 3.2. In Figure 5, we compare the mean, pointwise standard deviation and samples from the prior and the posterior distributions. As expected, we find that the data updates our belief about the spatially distributed parameter field and reduces the uncertainty. In particular, the 2σ bounds on the one-dimensional point marginals $\sigma(x)$, $\sigma_i = [\Gamma_{i,i}]^{-1/2}$ of the Gaussianized posterior and the prior distributions are shown, in order to verify that the samples are largely contained within two standard deviations of their respective means. The prior-preconditioned data-misfit Hessian $\mathbf{H}'_{\text{misfit}}$, is compressed using a relative tolerance of 10^{-6} , that is $\|\mathbf{H}'_{\text{misfit}} - \tilde{\mathbf{H}}'_{\text{misfit}}\|_2 / \|\mathbf{H}'_{\text{misfit}}\|_2 \leq 10^{-6}$, with high probability.

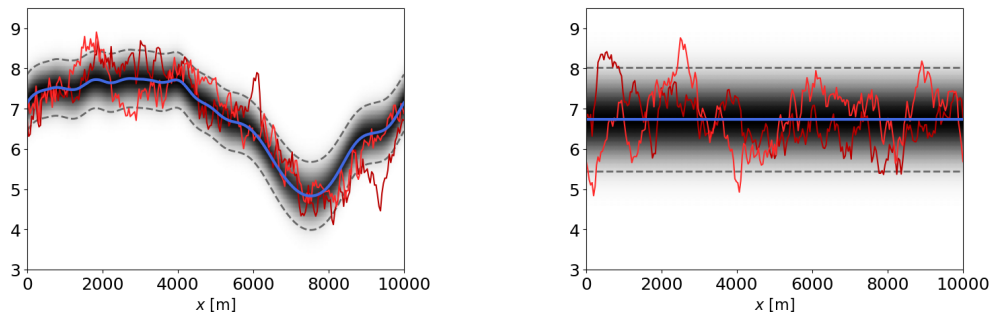


Figure 5: Results for Example I: Two random samples (red), mean $\bar{\beta}$ (blue) and boundaries of the region $R = \{(x, y) \text{ such that } 0 \leq x \leq W \text{ and } \bar{\beta}(x) - 2\sigma(x) \leq y \leq \bar{\beta}(x) + 2\sigma(x)\}$ (dashed black) are shown for the prior (left) and a HODLR Gaussianized posterior using the scheme described in Section 3.2 (right).

5.3. Dependence of Hessian block spectra on problem setting

Next, we study how problem features impact the numerical suitability of using global low-rank and HODLR compressions to approximate the Gauss-Newton data-misfit Hessian. In this and subsequent sections we measure the cost to generate the matrix compression in terms of Hessian vector products, which we also describe as Hessian applies, as each said vector product requires two linearized PDE solves and thus dominates the computational cost. We use the result of Appendix 8.2, to claim ε absolute error in a level L HODLR approximation, when there is no more than ε/L absolute error in each off-diagonal block. What is particular to this section, is that *adaptive* single-pass and HODLR algorithms are used to generate global low-rank and HODLR approximations, based on absolute tolerance criteria. The absolute tolerance algorithmic input is scaled by the largest global low-rank singular value in order to report relative approximation errors. We note that additional errors are neglected in the reported approximation error such as that incurred in the peeling process [11, 12] and additional approximation assumptions in the single-pass algorithm, both of which are not expected to be significant.

Influence of aspect ratio Here, we vary the aspect ratio of the domain $\phi = H/W$, where H and W are the domain height and width respectively, in order to study how it influences the block spectra of the Gauss-Newton data-misfit Hessian and ultimately the computational cost. Figure 6 shows that the global spectrum is more sensitive to changes in the relative length scale ϕ than the spectra of the off-diagonal blocks. Low-rank approximations of the off-diagonal blocks become computationally cheaper as ϕ decreases as a result of the sensitivity cones becoming increasingly localized as the ice sheet thickness decreases. Global low-rank approximations become more expensive as ϕ decreases, a result of the data being more informative. We note that realistic problems, such as the Humboldt glacier and the Greenland ice sheet studied later in Section 6,

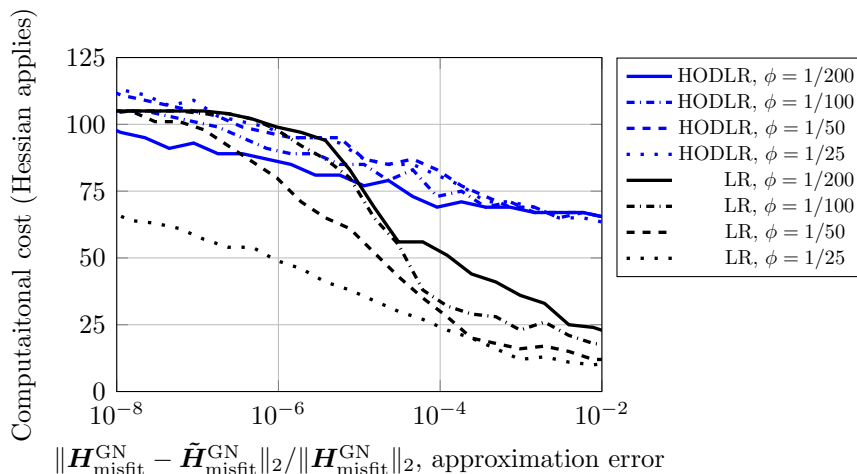


Figure 6: Comparison of HODLR and global low-rank (LR) compression costs of the Gauss-Newton data-misfit Hessian $\mathbf{H}_{\text{misfit}}^{\text{GN}}$, for Example I with ice sheet aspect ratio ϕ . This figure shows that for low aspect ratios, HODLR becomes more efficient than global low-rank for medium levels of target accuracy.

have small aspect ratios and are thus expected to have data-misfit Hessians that are less amenable to global low-rank approximation.

Influence of the parameter dimension We now vary the level of mesh discretization refinement in order to study the influence of data informativeness, through the discretized parameter dimension $N = \dim(\boldsymbol{\beta})$, on the computational cost to generate HODLR and global low-rank approximations of the Gauss-Newton data-misfit Hessian. The hierarchical depth L is incremented for every doubling of the discretized parameter dimension, in order that the hierarchical depth scales with the logarithm of the size of the Hessian matrix, a condition described in Section 2.2. Figure 7 provides computational evidence of the claim made in Section 2.2, that the number of applies needed to hierarchically compress an operator with HODLR structure is $\mathcal{O}(\log N)$. On the contrary, the number of applies to generate the global low-rank approximation is rather insensitive to the level of mesh refinement.

Influence of the data dimension Figure 8 shows that the global rank grows with the number of observations points and thus global low-rank compression tends to be less efficient for problems with strongly informative observation data. The rate of spectral decay of the (Gauss-Newton) data-misfit Hessian is related to the degree of ill-posedness of the unregularized inverse problem. As the number of observations increases, these associated model predictions are increasingly sensitive to small scale variations in the basal sliding field. Thus, more data, generally makes the data set more informative about the parameter and the (Gauss-Newton) data-misfit Hessian have a weaker rate of spectral decay.

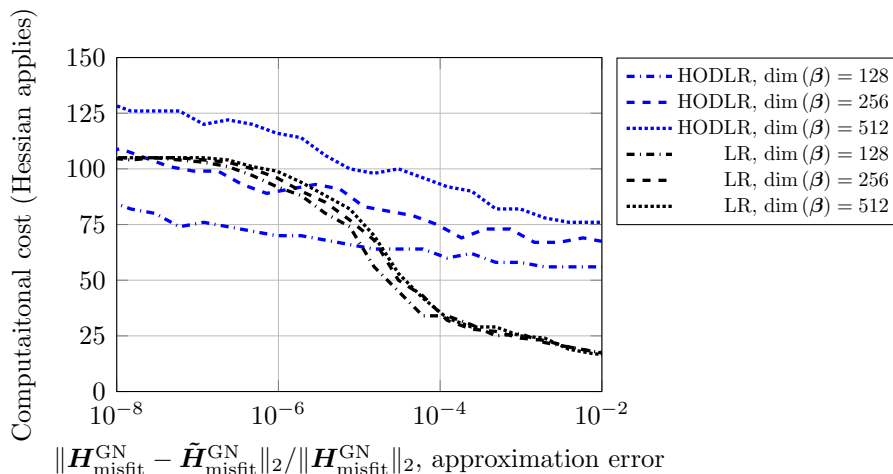


Figure 7: Dependence of HODLR and global low-rank (LR) compression costs of the Gauss-Newton data-misfit Hessian on $\dim(\beta)$, the dimension of the discretized logarithmic basal sliding field for Example I. The cost of global low-rank compression is almost constant, while the cost of HODLR compression increases as the mesh is refined.

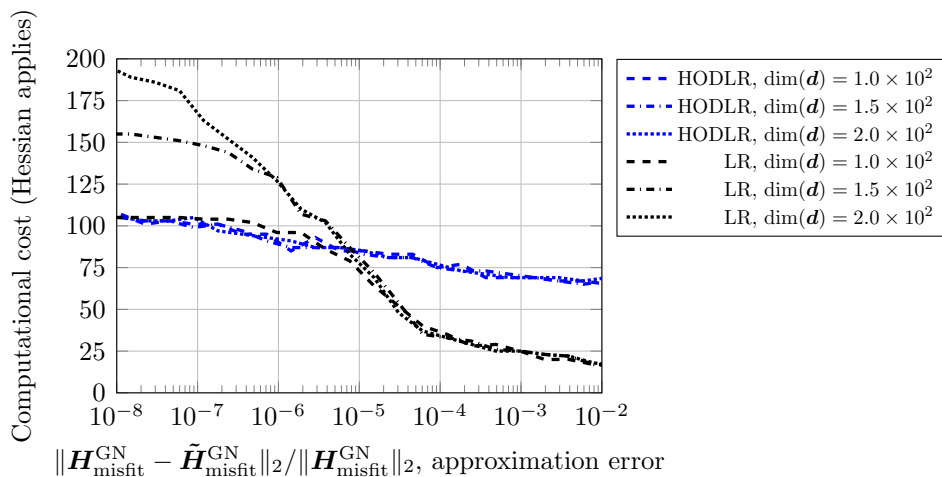


Figure 8: Dependence of HODLR and global low-rank (LR) compression costs of the Gauss-Newton data-misfit Hessian on $\dim(\mathbf{d})$, the data dimension, for Example I. The computational cost for global low-rank approximation increases with the number of observations, while the cost for HODLR compression is rather insensitive.

6. Example II: Humboldt glacier and Greenland ice sheet

Here, we study the scalability of the proposed methods using large-scale ice sheet problems which are typically used in climate simulations. Namely, we focus on the Humboldt glacier in North-West Greenland, and the entire Greenland ice sheet. For these simulations, we use the ice sheet model MALI, [46], which relies on

Albany, [47], a C++ multi-physics library for the implementation of the so-called first-order approximation of Stokes equations. This first-order approximation is based on scaling arguments motivated by the shallow nature of ice sheets and uses the incompressibility condition to reduce the unknowns to the horizontal velocities. We use PyAlbany [48] a convenient Python interface to the Albany package, which in turn builds upon Trilinos [49]. Albany is designed to support parallel and scalable finite-element discretized PDE solvers and various analysis capabilities. Details about the parameter, state, data dimensions as well as the number of cores and hierarchical levels used in the computations is provided in Table 1.

	Humboldt	Greenland
$\dim(\boldsymbol{\beta})$	11 608	320 116
$\dim(\mathbf{u})$	255 376	7 042 552
$\dim(\mathbf{d})$	23 216	640 232
# of cores	120	2 048
L	8	10

Table 1: Problem specifications for the Humboldt glacier and Greenland ice-sheet problems (Example II). Dimension of the discretized parameter field $\dim(\boldsymbol{\beta})$, dimension of the discretized velocity field $\dim(\mathbf{u})$, dimension of the observations $\dim(\mathbf{d})$, processors employed for computations and L depth of HODLR hierarchical partitioning.

The following study is partially motivated by findings made in the Section 5, namely that the role of the aspect ratio between the vertical and horizontal directions (see Section 5.3) influences the ability to use global low-rank compression and favors HODLR compression. We generate HODLR and global low-rank approximations and then based on the computed spectra, Equation 3 and $\zeta^{\text{LR}} = r + d$, we estimate the computational cost. Additionally, we study how the ordering of the degrees of freedom impacts the spectral decay for off-diagonal blocks of the data-misfit Hessian. We present results for both, the Humboldt glacier, which expands about 4×10^2 [km] laterally, and the Greenland ice sheet, which expands about 1.8×10^3 [km]. The ice is at most 3.4 [km] thick, resulting in approximate aspect ratios of 8.5×10^{-3} for Humboldt and 1.9×10^{-3} for Greenland. We use a nonuniform triangulation of the Greenland ice sheet, with mesh size ranging from 1 to 10 [km], and we then extrude it in the vertical direction, obtaining a 3D mesh having 10 layers of prismatic elements. The velocity observations at the top surface of the Greenland ice sheet are obtained from satellite observations [50]. The MAP basal sliding field and the temperature fields are obtained as part of the initialization process, using a numerical optimization approach to match the ice velocity observations and constrained by the first-order flow model coupled with a temperature model [51]. Additional details about the mesh geometries and data, in particular regarding the Humboldt glacier, can be found in [52].

In Figure 9, we show the observed surface velocity \mathbf{d} in [m/yr], the MAP estimates

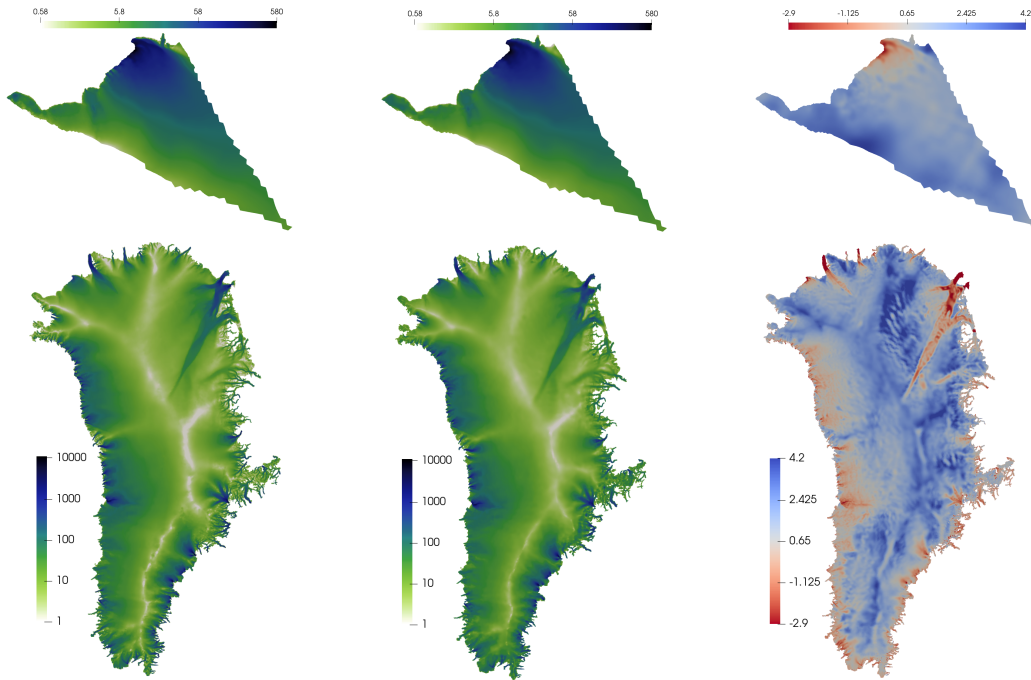


Figure 9: Data and MAP estimates for Example II. Shown are the surface velocity observation data (left), and the reconstructed surface velocity field (middle) that is based on the MAP estimate of the logarithmic basal sliding field (right). Top row is for the Humboldt glacier and bottom row for the Greenland ice sheet.

of the logarithmic basal sliding field β^* ($\exp(\beta^*)$ is in [kPa yr/m]) and surface velocity in [m/yr] generated by the model.

6.1. HODLR compressability

We next generate global low-rank approximations of a Greenland and Humboldt data-misfit Hessian as well as low-rank approximations of various off-diagonal blocks. Plots of the estimated singular values are provided in Figure 10. We observe that the spectrum of the Greenland ice sheet decays substantially slower than the one for the Humboldt glacier. Besides the different sizes of these two discretized problems, this is also due to the different aspect ratios. Having estimated singular values of the data-misfit Hessians and the appropriate off-diagonal blocks, one is able to estimate computational costs to compress them into the global low-rank and HODLR matrix formats. The computational cost as a function of Hessian approximation target accuracy is given in Figure 11, wherein it is demonstrated that the HODLR compression format can offer a favorable means to approximate data-misfit Hessians for large-scale inverse problems governed by complex ice-sheet models.

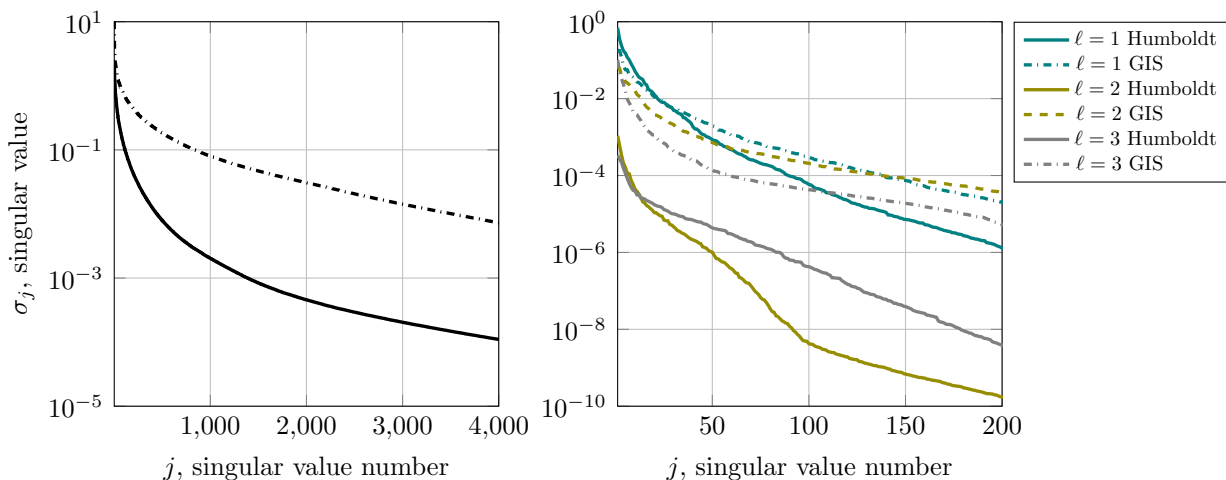


Figure 10: Singular values of the data-misfit Hessian (left figure) and various off-diagonal blocks of the data-misfit Hessian (right figure) for Example II. The color-scheme in the right most figure is consistent with Figure 1. On the left, the singular values of the Humboldt and Greenland data-misfit Hessians are shown using a solid and dash-dotted line, respectively. On the right, we show the singular values of the upper most blocks, that is $\mathbf{A}_{1,2}^{(\ell)}$ as defined in Section 8.2.

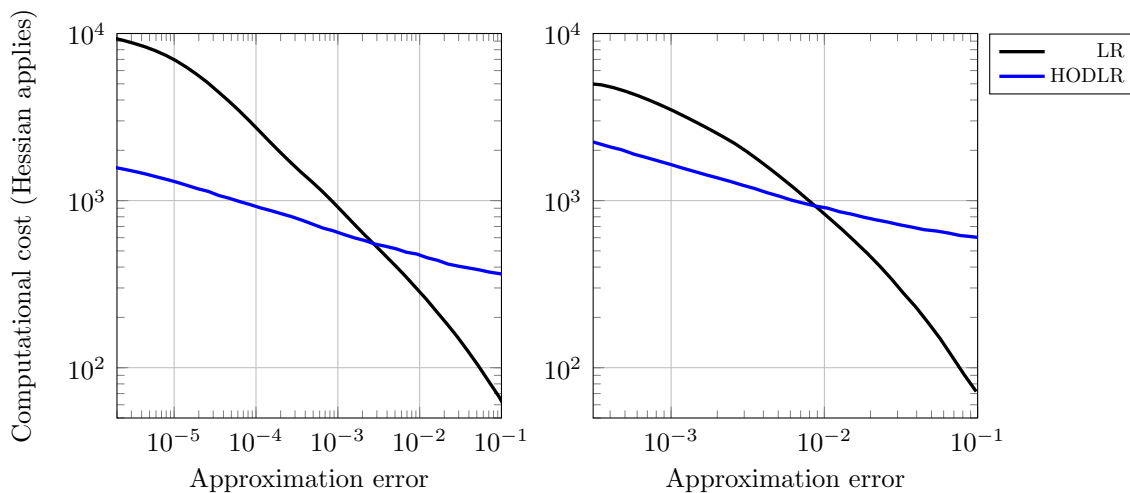


Figure 11: Estimated computational costs (measured by the number of Hessian applies) to compress the Humboldt glacier (left) and Greenland ice-sheet (right) data-misfit Hessians into the global low-rank (LR) and hierarchical off-diagonal low-rank (HODLR) formats as a function of the approximation error $\|\mathbf{H}_{\text{misfit}} - \tilde{\mathbf{H}}_{\text{misfit}}\|_2 / \|\mathbf{H}_{\text{misfit}}\|_2$.

6.2. Impact of parameter degree of freedom ordering

We seek to ensure that the off-diagonal blocks, determined by the hierarchical partitioning described in Section 2.2, of the data-misfit Hessian are low-rank. For

this reason, the nodes $\{\mathbf{x}_i\}_i$ associated to the degrees of freedom (dofs) are ordered according to a kd-tree, i.e., a recursive hyperplane splitting. The ordering provided by the kd-tree is such that the (i, j) -entry of the distance matrix $\mathbf{D}_{i,j} = \|\mathbf{x}_i - \mathbf{x}_j\|_2$, is typically small whenever $|i - j|$ is small, that is the dof ordering preserves some notion of locality (see Section 3.1). In particular, a sparse permutation matrix \mathbf{B} , is determined, whose action reorders the dofs from the default ordering provided by the finite element discretization to that specified by the kd-tree. The data-misfit Hessian with respect to the kd-tree ordering, $\mathbf{H}_{\text{misfit}}^{\text{kd}} := \mathbf{B}\mathbf{H}_{\text{misfit}}\mathbf{B}^\top$, is then amenable to HODLR compression. Subsequently, $\mathbf{B}^\top \tilde{\mathbf{H}}_{\text{misfit}}^{\text{kd}} \mathbf{B}$ is an approximation of the data-misfit Hessian with respect to the default ordering.

The dof ordering has no impact on a matrix’s global numerical rank but does indeed impact the numerical rank of its numerous submatrices that are defined by a fixed partitioning scheme, such as the off-diagonal blocks of an HODLR matrix (see Section 2.2). Here, we study the HODLR compressibility of the Humboldt glacier data-misfit Hessian by comparing the rate of decay of an off-diagonal block’s singular values using the default ordering provided by Albany and the ordering obtained by a kd-tree recursive hyperplane splitting. As observed in Figure 12, the rate at which the singular values of the level-1 off-diagonal block decay, strongly depends on the dof ordering. This is because the ordering given by the kd-tree better preserves locality, and as a consequence, by the argument provided in Section 3.1, the singular values decay much faster when using the kd-tree ordering. The kd-tree ordering therefore provides a substantially computationally cheaper means to generate an HODLR approximation of the data-misfit Hessian. Figure 12 also shows distance matrices for the default and kd-tree bases. These show the improved locality for the kd-orderings. Note that data-misfit Hessian matrices are expected to follow a similar structure as these distance matrices, which explains why the former’s off-diagonal blocks can be compressed more effectively in the kd-order than in the default order of dofs.

7. Conclusion

In this work, we motivated why data-misfit Hessians which arise from a class of inverse problems governed by PDEs have HODLR matrix structure. HODLR matrices can efficiently be inverted and factorized, operations needed for solving inverse problems governed by PDEs by Newton’s method, for constructing Gaussian approximations and for Markov chain Monte Carlo sampling methods. We study inverse ice sheet problems, for which, under certain regimes, HODLR matrices provide a more computationally efficient approximation format than the global low-rank matrix format. These problems are those with highly informative data and small aspect ratio ice sheets. While global low-rank matrices are favorable for large discretized parameter dimension and small data dimension, we find that HODLR matrices can offer computational savings for large-scale inverse problems such as a Greenland ice sheet inverse problem with satellite observational data and a discretized parameter dimension that exceeds 10^5 .

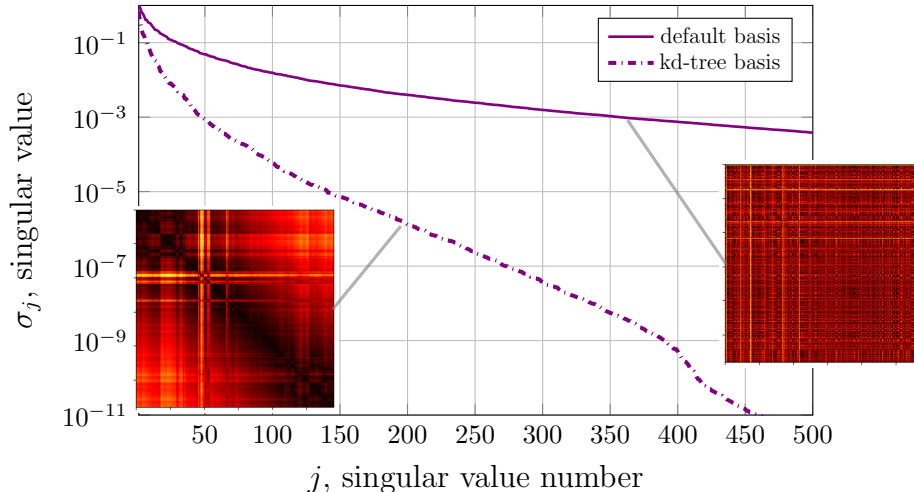


Figure 12: Singular values of the hierarchical level 1 off-diagonal block, $\mathbf{A}_{1,2}^{(1)}$, of the Humboldt glacier data-misfit Hessian, when expressed in a kd-tree basis and the default basis. Shown also are heat maps of the distance matrices $\mathbf{D}_{i,j} = \|\mathbf{x}_i - \mathbf{x}_j\|_2$, wherein the nodes $\{\mathbf{x}_i\}_i$, associated to the finite element degrees of freedom have been ordered according to a default standard and a kd-tree.

For future work, we believe that the computational cost can be reduced further by utilizing hierarchical matrix partitionings that satisfy a strong admissibility condition [17], as they are better suited to exploit data-misfit Hessian structure. However, generating a hierarchical matrix approximation with such a partitioning, e.g., by the peeling method [11, 12], requires substantially more Hessian vector products. Ultimately, to further reduce the computational cost of Hessian approximations in inverse problems governed by PDEs, exploiting further problem structure will be essential.

8. Appendix

8.1. Randomized Compression Algorithms

Here, for completeness we outline the randomized matrix-free double-pass global low-rank and HODLR compression algorithms. The essential ideas of the randomized double-pass low-rank algorithm [32] are

- (i) the application of a vector $\boldsymbol{\omega}$ with random entries to a matrix \mathbf{A} , yields a vector $\mathbf{y} = \mathbf{A}\boldsymbol{\omega}$, which is likely aligned with the dominant left singular vectors of \mathbf{A} ;
- (ii) a matrix \mathbf{Q} , whose columns are nearly aligned with the dominant left singular vectors of \mathbf{A} , can be used to construct an accurate low-rank approximation

$$\tilde{\mathbf{A}} = \mathbf{Q}\mathbf{Q}^\top \mathbf{A} \text{ of } \mathbf{A}.$$

The double-pass randomized SVD algorithm is presented in Algorithm 1 and does not significantly differ from that in [32], specifically it is lines 7, 8 and 9 that are distinct. This minor modification frees us from the need to compute a (parallel) singular value decomposition (SVD) of a (distributed) $N \times k$ matrix, such as \mathbf{Z} . Here, we only need to compute an SVD of the smaller $k \times k$ matrix \mathbf{R}_Z . In the distributed memory parallelism setting of Section 6, this algorithmic modification allows us to only require the invocation of serial SVD routines, as \mathbf{R}_Z , which is typically small, is available on each processor.

Algorithm 1 Double-pass randomized SVD.

Input: $\mathbf{A} \in \mathbb{R}^{N \times N}$, $r \in \mathbb{N}$ desired rank and oversampling parameter $d \in \mathbb{N}$.

Output: low-rank approximation $\tilde{\mathbf{A}}$ of \mathbf{A}

1:	$k = r + d$	
2:	$\mathbf{\Omega} = \text{randn}(N, k)$	{Initiate random matrix}
3:	$\mathbf{Y} = \mathbf{A}\mathbf{\Omega}$	{Sample column space}
4:	$\mathbf{Q}_Y = \text{orthog}(\mathbf{Y})$	{Orthogonalize column samples}
5:	$\mathbf{Z} = \mathbf{A}^\top \mathbf{Q}_Y$	{Sample row space}
6:	$\mathbf{Q}_Z = \text{orthog}(\mathbf{Z})$	{Orthogonalize row samples}
7:	$\mathbf{R}_Z = \mathbf{Q}_Z^\top \mathbf{Z}$	{Compress row samples}
8:	$\mathbf{R}_Z = \hat{\mathbf{V}}\mathbf{\Sigma}\hat{\mathbf{U}}^\top$	{SVD of $k \times k$ compressed row sample matrix}
9:	$\mathbf{V} = \mathbf{Q}_Z \hat{\mathbf{V}}$	{Project row space information}
10:	$\mathbf{U} = \mathbf{Q}_Y \hat{\mathbf{U}}$	{Project column space information}
11:	$\tilde{\mathbf{A}} = \mathbf{U}\mathbf{\Sigma}\mathbf{V}^\top$	{Form low-rank approximation}

The randomized hierarchical off-diagonal low-rank algorithm proceeds by compressing off-diagonal blocks by the double-pass algorithm. The larger off-diagonal blocks are compressed prior to the compression of smaller off-diagonal blocks, via a peeling procedure [11]. Here, both \mathbf{A} and $\tilde{\mathbf{A}}$ are assumed to be symmetric as we seek compression of symmetric operators and computation of symmetric approximants.

Algorithm 2 Symmetric matrix-free randomized HODLR.

Input: symmetric $\mathbf{A} \in \mathbb{R}^{N \times N}$, hierarchical depth $L \in \mathbb{N}$, r_1, \dots, r_L desired ranks of the off-diagonal blocks at each hierarchical depth and oversampling parameter d .

Output: symmetric HODLR approximation $\tilde{\mathbf{A}}$ of \mathbf{A}

```

1: for  $\ell = 1, 2, \dots, L$  do
2:    $k_\ell = r_\ell + d$ 
3:    $\mathbf{\Omega} = \text{zeros}(N, k_\ell)$ 
4:   for  $j = 1, \dots, 2^{\ell-1}$  do
5:      $\mathbf{\Omega}(\mathcal{I}_{2j}^{(\ell)}, :) = \text{randn}(|\mathcal{I}_{2j}^{(\ell)}|, k_\ell)$            {Initiate structured random matrix}
6:   end for
7:    $\mathbf{Y} = \left( \mathbf{A} - \sum_{j=1}^{\ell-1} \mathbf{A}^{(j)} \right) \mathbf{\Omega}$            {Sample off-diagonal block column spaces}
8:   for  $j = 1, \dots, 2^{\ell-1}$  do
9:      $\mathbf{Y}^{(j)} = \text{zeros}(N, k_\ell)$ 
10:     $\mathbf{Y}^{(j)}(\mathcal{I}_{2j-1}^{(\ell)}, :) = \mathbf{Y}(\mathcal{I}_{2j-1}^{(\ell)}, :)$ 
11:     $\mathbf{Q}_{\mathbf{Y}}^{(j)} = \text{orthog}(\mathbf{Y}^{(j)})$            {Orthogonalize column samples of the level  $\ell$ 
      off-diagonal blocks}
12:   end for
13:    $\mathbf{Q}_{\mathbf{Y}} = \sum_{j=1}^{2^{\ell-1}} \mathbf{Q}_{\mathbf{Y}}^{(j)}$            {Row space sampling matrix}
14:    $\mathbf{Z} = \left( \mathbf{A} - \sum_{j=1}^{\ell-1} \mathbf{A}^{(j)} \right) \mathbf{Q}_{\mathbf{Y}}$            {Sample off-diagonal block row spaces}
15:   for  $j = 1, \dots, 2^{\ell-1}$  do
16:      $\mathbf{Z}^{(j)} = \mathbf{Z}(\mathcal{I}_{2j}^{(\ell)}, :)$ 
17:      $\mathbf{Q}_{\mathbf{Z}}^{(j)} = \text{orthog}(\mathbf{Z}^{(j)})$            {Orthogonalize row samples of the level  $\ell$  off-diagonal
      blocks}
18:      $\mathbf{R}_{\mathbf{Z}}^{(j)} = \left( \mathbf{Q}_{\mathbf{Z}}^{(j)} \right)^\top \mathbf{Z}^{(j)}$            {Compress level  $\ell$  off-diagonal block row samples}
19:      $\mathbf{R}_{\mathbf{Z}}^{(j)} = \hat{\mathbf{V}}_{2j-1}^{(\ell)} \mathbf{\Sigma}_{2j-1}^{(\ell)} \hat{\mathbf{U}}_{2j-1}^{(\ell)}$            {SVD of  $k_\ell \times k_\ell$  compressed row sample matrix}
20:      $\mathbf{V}_{2j-1}^{(\ell)} = \mathbf{Q}_{\mathbf{Z}}^{(j)} \hat{\mathbf{V}}_{2j-1}^{(\ell)}$            {Project row space information}
21:      $\mathbf{U}_{2j-1}^{(\ell)} = \mathbf{Q}_{\mathbf{Y}}^{(j)} \hat{\mathbf{U}}_{2j-1}^{(\ell)}$            {Project column space information}
22:      $\mathbf{V}_{2j}^{(\ell)} = \mathbf{U}_{2j-1}^{(\ell)}$ 
23:      $\mathbf{U}_{2j}^{(\ell)} = \mathbf{V}_{2j-1}^{(\ell)}$ 
24:      $\mathbf{\Sigma}_{2j}^{(\ell)} = \mathbf{\Sigma}_{2j-1}^{(\ell)}$ 
25:   end for
26:    $\mathbf{A}^{(\ell)} = \sum_{j=1}^{2^\ell} \mathbf{U}_j^{(\ell)} \mathbf{\Sigma}_j^{(\ell)} \left( \mathbf{V}_j^{(\ell)} \right)^\top$ 
27: end for
28: obtain block diagonal  $\mathbf{D}$  of  $\mathbf{A}$  by sampling  $\mathbf{A} - \sum_{j=1}^L \mathbf{A}^{(j)}$ 
29:  $\tilde{\mathbf{A}} = \mathbf{D} + \sum_{\ell=1}^L \mathbf{A}^{(\ell)}$ 

```

8.2. Global HODLR approximation error from the accumulation of block low-rank off-diagonal approximation errors

Let \mathbf{A} be a $N \times N$ matrix and consider the following partitioning

$$\begin{aligned} \mathbf{A}^{(1)} &= \begin{pmatrix} \mathbf{0} & \mathbf{A}_{1,2}^{(1)} \\ \mathbf{A}_{2,1}^{(1)} & \mathbf{0} \end{pmatrix}, \\ \mathbf{A}^{(2)} &= \begin{pmatrix} \mathbf{0} & \mathbf{A}_{1,2}^{(2)} & \mathbf{0} & \mathbf{0} \\ \mathbf{A}_{2,1}^{(2)} & \mathbf{0} & \mathbf{0} & \mathbf{0} \\ \mathbf{0} & \mathbf{0} & \mathbf{0} & \mathbf{A}_{3,4}^{(2)} \\ \mathbf{0} & \mathbf{0} & \mathbf{A}_{4,3}^{(2)} & \mathbf{0} \end{pmatrix}, \\ \mathbf{D} &= \begin{pmatrix} \mathbf{A}_{1,1}^{(2)} & \mathbf{0} & \mathbf{0} & \mathbf{0} \\ \mathbf{0} & \mathbf{A}_{2,2}^{(2)} & \mathbf{0} & \mathbf{0} \\ \mathbf{0} & \mathbf{0} & \mathbf{A}_{3,3}^{(2)} & \mathbf{0} \\ \mathbf{0} & \mathbf{0} & \mathbf{0} & \mathbf{A}_{4,4}^{(2)} \end{pmatrix}, \end{aligned}$$

where $\mathbf{A}_{i,j}^{(\ell)}$ is the (i,j) block of a $2^\ell \times 2^\ell$ block partitioning of \mathbf{A} , where $1 \leq \ell \leq L$. $\mathbf{A}^{(\ell)}$ contains all blocks $\mathbf{A}_{i,j}^{(\ell)}$ such that $|i-j|=1$ and \mathbf{D} contains the diagonal blocks $\mathbf{A}_{i,i}^{(L)}$. Above, we show the decomposition $\mathbf{A} = \sum_{\ell=1}^L \mathbf{A}^{(\ell)} + \mathbf{D}$ for $L=2$ hierarchical depth but in the following analysis L is arbitrary. Let $\mathbf{x} \in \mathbb{R}^N$, then

$$\begin{aligned} \mathbf{A}\mathbf{x} &= \sum_{j=1}^L \mathbf{A}^{(j)}\mathbf{x} + \mathbf{D}\mathbf{x}, \\ \mathbf{A}^{(1)}\mathbf{x} &= \begin{pmatrix} \mathbf{A}_{1,2}^{(1)}\mathbf{x}_2^{(1)} \\ \mathbf{A}_{2,1}^{(1)}\mathbf{x}_1^{(1)} \end{pmatrix}, \quad \mathbf{x} = \begin{pmatrix} \mathbf{x}_1^{(1)} \\ \mathbf{x}_2^{(2)} \end{pmatrix}, \\ \mathbf{A}^{(j)}\mathbf{x} &= \begin{pmatrix} \mathbf{A}_{1,2}^{(j)}\mathbf{x}_2^{(j)} \\ \mathbf{A}_{2,1}^{(j)}\mathbf{x}_1^{(j)} \\ \vdots \\ \mathbf{A}_{2^{j-1},2^j}^{(j)}\mathbf{x}_{2^j}^{(j)} \\ \mathbf{A}_{2^j,2^{j-1}}^{(j)}\mathbf{x}_{2^{j-1}}^{(j)} \end{pmatrix}, \quad \mathbf{x} = \begin{pmatrix} \mathbf{x}_1^{(j)} \\ \mathbf{x}_2^{(j)} \\ \vdots \\ \mathbf{x}_{2^{j-1}}^{(j)} \\ \mathbf{x}_{2^j}^{(j)} \end{pmatrix}, \end{aligned}$$

from which we obtain the following expression

$$\|\mathbf{A}^{(j)}\mathbf{x}\|_2^2 = \sum_{k=1}^{2^{j-1}} \left(\|\mathbf{A}_{2^{k-1},2^k}^{(j)}\mathbf{x}_{2^k}^{(j)}\|_2^2 + \|\mathbf{A}_{2^k,2^{k-1}}^{(j)}\mathbf{x}_{2^{k-1}}^{(j)}\|_2^2 \right).$$

Now assume that $\tilde{\mathbf{A}}$ is an HODLR approximation of \mathbf{A} , whose diagonal \mathbf{D} is equal to the diagonal of \mathbf{A} so that

$$\begin{aligned} (\mathbf{A} - \tilde{\mathbf{A}}) &= \sum_{j=1}^L \Delta\mathbf{A}^{(j)}, \\ \Delta\mathbf{A}^{(j)} &:= (\mathbf{A}^{(j)} - \tilde{\mathbf{A}}^{(j)}). \end{aligned}$$

Here we assume each off-diagonal block has been approximated to some absolute tolerance $\varepsilon > 0$, so that $\|\Delta\mathbf{A}_{2^{k-1},2^k}^{(j)}\|_2, \|\Delta\mathbf{A}_{2^k,2^{k-1}}^{(j)}\|_2 \leq \varepsilon$ for each $j = 1, 2, \dots, L$ and

$k = 1, 2, \dots, 2^{j-1}$. For $\mathbf{x} \in \mathbb{R}^N$ we have

$$\begin{aligned} \left\| \left(\mathbf{A} - \tilde{\mathbf{A}} \right) \mathbf{x} \right\|_2 &\leq \sum_{j=1}^L \left\| \Delta \mathbf{A}^{(j)} \mathbf{x} \right\|_2, \\ \left\| \Delta \mathbf{A}^{(j)} \mathbf{x} \right\|_2 &= \sqrt{\sum_{k=1}^{2^{j-1}} \left(\left\| \Delta \mathbf{A}_{2^{k-1}, 2^k}^{(j)} \mathbf{x}_{2^k}^{(j)} \right\|_2^2 + \left\| \Delta \mathbf{A}_{2^k, 2^{k-1}}^{(j)} \mathbf{x}_{2^{k-1}}^{(j)} \right\|_2^2 \right)} \\ &\leq \sqrt{\sum_{k=1}^{2^{j-1}} \left(\varepsilon^2 \left\| \mathbf{x}_{2^k}^{(j)} \right\|_2^2 + \varepsilon^2 \left\| \mathbf{x}_{2^{k-1}}^{(j)} \right\|_2^2 \right)}, \\ \left\| \Delta \mathbf{A}^{(j)} \mathbf{x} \right\|_2 &\leq \varepsilon \sqrt{\sum_{k=1}^{2^{j-1}} \left(\left\| \mathbf{x}_{2^k}^{(j)} \right\|_2^2 + \left\| \mathbf{x}_{2^{k-1}}^{(j)} \right\|_2^2 \right)} = \varepsilon \left\| \mathbf{x} \right\|_2, \\ \left\| \left(\mathbf{A} - \tilde{\mathbf{A}} \right) \mathbf{x} \right\|_2 &\leq \varepsilon L \left\| \mathbf{x} \right\|_2, \\ \left\| \mathbf{A} - \tilde{\mathbf{A}} \right\|_2 &:= \sup_{\mathbf{x} \neq \mathbf{0}} \left(\frac{\left\| \left(\mathbf{A} - \tilde{\mathbf{A}} \right) \mathbf{x} \right\|_2}{\left\| \mathbf{x} \right\|_2} \right) \leq \varepsilon L. \end{aligned}$$

8.3. Error analysis for posterior-covariance

Consider a symmetric matrix $\mathbf{A} \in \mathbb{R}^{N \times N}$, whose eigenvalues are bounded below by a number greater than -1 and a symmetric approximant $\tilde{\mathbf{A}}$, with discrepancy $\Delta \mathbf{A} = \mathbf{A} - \tilde{\mathbf{A}}$. We signify a generic eigenvalue of \mathbf{S} by $\lambda(\mathbf{S})$ so that $s_1 \leq \lambda(\mathbf{S}) \leq s_2$ indicates that all eigenvalues of \mathbf{S} are bounded below by s_1 and above by s_2 . Now we provide a bound for the error of $(\mathbf{I} + \mathbf{A})^{-1} - (\mathbf{I} + \tilde{\mathbf{A}})^{-1}$, given that $\|\Delta \mathbf{A}\|_2 = \varepsilon$, so that one may assess the accuracy of an HODLR Gaussianized posterior covariance. When, as in Section 3.2, \mathbf{A} is the prior-preconditioned Hessian misfit, $\|(\mathbf{I} + \mathbf{A})^{-1} - (\mathbf{I} + \tilde{\mathbf{A}})^{-1}\|_2$ quantifies the discrepancy between an HODLR approximate Gaussianized posterior covariance and the true Gaussianized posterior covariance.

$$\begin{aligned} (\mathbf{I} + \mathbf{A})^{-1} - (\mathbf{I} + \tilde{\mathbf{A}})^{-1} &= (\mathbf{I} + \mathbf{A})^{-1} - (\mathbf{I} + \mathbf{A} - \Delta \mathbf{A})^{-1} = \\ &= (\mathbf{I} + \mathbf{A})^{-1} - \left((\mathbf{I} + \mathbf{A}) (\mathbf{I} - (\mathbf{I} + \mathbf{A})^{-1} \Delta \mathbf{A}) \right)^{-1} = \\ &= (\mathbf{I} + \mathbf{A})^{-1} - \left(\mathbf{I} - (\mathbf{I} + \mathbf{A})^{-1} \Delta \mathbf{A} \right)^{-1} (\mathbf{I} + \mathbf{A})^{-1} = \\ &= \left(\mathbf{I} - (\mathbf{I} - (\mathbf{I} + \mathbf{A})^{-1} \Delta \mathbf{A})^{-1} \right) (\mathbf{I} + \mathbf{A})^{-1}. \end{aligned}$$

Given that $\|\Delta \mathbf{A}\|_2 = \varepsilon$, we have

$$\begin{aligned} -\varepsilon &\leq \lambda(\Delta \mathbf{A}) \leq \varepsilon, \\ -\varepsilon^* &\leq \lambda\left((\mathbf{I} + \mathbf{A})^{-1} \Delta \mathbf{A}\right) \leq \varepsilon^*, \\ \varepsilon^* &:= \varepsilon(1 + \lambda_{\min}(\mathbf{A}))^{-1}, \\ 1 + \varepsilon^* &\geq \lambda\left(\mathbf{I} - (\mathbf{I} + \mathbf{A})^{-1} \Delta \mathbf{A}\right) \geq 1 - \varepsilon^*, \end{aligned}$$

we next assume $\varepsilon^* < 1$, so that the eigenvalues of $\mathbf{I} - (\mathbf{I} + \mathbf{A})^{-1} \Delta \mathbf{A}$ are necessarily positive and

$$(1 + \varepsilon^*)^{-1} \leq \lambda \left((\mathbf{I} - (\mathbf{I} + \mathbf{A})^{-1} \Delta \mathbf{A})^{-1} \right) \leq (1 - \varepsilon^*)^{-1}.$$

With this it follows that

$$\begin{aligned} \|(\mathbf{I} + \mathbf{A})^{-1} - (\mathbf{I} + \tilde{\mathbf{A}})^{-1}\|_2 / \|(\mathbf{I} + \mathbf{A})^{-1}\|_2 &\leq (1 - (1 + \varepsilon^*)^{-1}) \\ \|(\mathbf{I} + \mathbf{A})^{-1} - (\mathbf{I} + \tilde{\mathbf{A}})^{-1}\|_2 / \|(\mathbf{I} + \mathbf{A})^{-1}\|_2 &\leq \frac{\varepsilon^*}{1 + \varepsilon^*}, \end{aligned}$$

where, as before $\varepsilon^* = \|\Delta \mathbf{A}\|_2 / (1 + \lambda_{\min}(\mathbf{A}))$.

Acknowledgments

The authors thank Trevor Hillebrand from Los Alamos National Laboratory for help with setting up the Humboldt and Greenland ice-sheet grids and datasets. Support for this work was provided by the National Science Foundation under Grant No. DMS-1840265 and CAREER-1654311 and through the SciDAC project ProSPect, funded by the U.S. Department of Energy (DOE) Office of Science, Advanced Scientific Computing Research and Biological and Environmental Research programs. This research used resources of the National Energy Research Scientific Computing Center (NERSC), a U.S. Department of Energy Office of Science User Facility operated under Contract No. DE-AC02-05CH11231, under NERSC award ERCAP0020130.

Disclaimer

This paper describes objective technical results and analysis. Any subjective views or opinions that might be expressed in the paper do not necessarily represent the views of the U.S. Department of Energy or the United States Government. Sandia National Laboratories is a multimission laboratory managed and operated by National Technology and Engineering Solutions of Sandia, LLC, a wholly owned subsidiary of Honeywell International, Inc., for the U.S. Department of Energy's National Nuclear Security Administration under contract DE-NA-0003525.

References

- [1] Isaac T, Petra N, Stadler G and Ghattas O 2015 Scalable and efficient algorithms for the propagation of uncertainty from data through inference to prediction for large-scale problems, with application to flow of the Antarctic ice sheet *Journal of Computational Physics* **296** 348–368
- [2] Petra N, Martin J, Stadler G and Ghattas O 2014 A computational framework for infinite-dimensional Bayesian inverse problems: Part II. Stochastic Newton MCMC with application to ice sheet flow inverse problems *SIAM Journal on Scientific Computing* **36** A1525–A1555
- [3] Spantini A, Solonen A, Cui T, Martin J, Tenorio L and Marzouk Y 2015 Optimal low-rank approximations of Bayesian linear inverse problems *SIAM Journal on Scientific Computing* **37** A2451–A2487

- [4] Flath H P, Wilcox L C, Akçelik V, Hill J, van Bloemen Waanders B and Ghattas O 2011 Fast algorithms for Bayesian uncertainty quantification in large-scale linear inverse problems based on low-rank partial Hessian approximations *SIAM Journal on Scientific Computing* **33** 407–432
- [5] Bui-Thanh T, Ghattas O, Martin J and Stadler G 2013 A computational framework for infinite-dimensional Bayesian inverse problems Part I: The linearized case, with application to global seismic inversion *SIAM Journal on Scientific Computing* **35** A2494–A2523
- [6] Saibaba A K and Kitanidis P K 2015 Fast computation of uncertainty quantification measures in the geostatistical approach to solve inverse problems *Advances in Water Resources* **82** 124–138
- [7] Martinsson P G 2011 A fast randomized algorithm for computing a hierarchically semiseparable representation of a matrix *SIAM Journal on Matrix Analysis and Applications* **32** 1251–1274
- [8] Alger N, Rao V, Meyers A, Bui-Thanh T and Ghattas O 2019 Scalable matrix-free adaptive product-convolution approximation for locally translation-invariant operators *SIAM Journal on Scientific Computing* **41** A2296–A2328
- [9] Alger N, Hartland T, Petra N and Ghattas O Efficient matrix-free point spread function approximation of operators with locally supported non-negative integral kernels, with application to Hessians in PDE constrained inverse problems To be submitted
- [10] Zhu H, Li S, Fomel S, Stadler G and Ghattas O 2016 A Bayesian approach to estimate uncertainty for full waveform inversion with a priori information from depth migration *Geophysics* **81** R307–R323
- [11] Lin L, Lu J and Ying L 2011 Fast construction of hierarchical matrix representation from matrix–vector multiplication *Journal of Computational Physics* **230** 4071–4087
- [12] Martinsson P G 2016 Compressing rank-structured matrices via randomized sampling *SIAM Journal on Scientific Computing* **38** A1959–A1986
- [13] Geoga C J, Anitescu M and Stein M L 2020 Scalable Gaussian process computations using hierarchical matrices *Journal of Computational and Graphical Statistics* **29** 227–237
- [14] Litvinenko A, Sun Y, Genton M G and Keyes D E 2019 Likelihood approximation with hierarchical matrices for large spatial datasets *Computational Statistics & Data Analysis* **137** 115–132
- [15] Ambartsumyan I, Boukaram W, Bui-Thanh T, Ghattas O, Keyes D, Stadler G, Turkiyyah G and Zampini S 2020 Hierarchical matrix approximations of Hessians arising in inverse problems governed by PDEs *SIAM Journal on Scientific Computing* **42** A3397–A3426
- [16] Hackbusch W 1999 A sparse matrix arithmetic based on \mathcal{H} -matrices. Part I: Introduction to \mathcal{H} -matrices *Computing* **62** 89–108
- [17] Hackbusch W and Börm S 2002 Data-sparse approximation by adaptive \mathcal{H}^2 -matrices *Computing* **69** 1–35
- [18] Tarantola A 2005 *Inverse problem theory and methods for model parameter estimation* (SIAM)
- [19] Kaipio J and Somersalo E 2006 *Statistical and computational inverse problems* vol 160 (Springer Science & Business Media)
- [20] Stuart A M 2010 Inverse problems: A Bayesian perspective *Acta Numerica* **19** 451–559
- [21] Nocedal J and Wright S J 2006 *Numerical Optimization* 2nd ed (Berlin, Heidelberg, New York: Springer Verlag)
- [22] Borzi A and Schulz V 2011 *Computational optimization of systems governed by partial differential equations* (SIAM)
- [23] Gunzburger M D 2002 *Perspectives in flow control and optimization* (SIAM)
- [24] Petra N and Sachs E W 2021 Second order adjoints in optimization *Numerical Analysis and Optimization* ed Al-Baali M, Purnama A and Grandinetti L (Cham: Springer International Publishing) pp 209–230
- [25] Hastings W K 1970 Monte Carlo sampling methods using Markov chains and their applications *Biometrika* **57** 97–109
- [26] Robert C P, Casella G and Casella G 1999 *Monte Carlo statistical methods* vol 2 (Springer)
- [27] Rudolf D and Sprungk B 2018 On a generalization of the preconditioned Crank–Nicolson Metropolis algorithm *Foundations of Computational Mathematics* **18** 309–343

- [28] Pinski F J, Simpson G, Stuart A M and Weber H 2015 Algorithms for Kullback–Leibler approximation of probability measures in infinite dimensions *SIAM Journal on Scientific Computing* **37** A2733–A2757
- [29] Kim K T, Villa U, Parno M, Marzouk Y, Ghattas O and Petra N 2021 hIPPYlib-MUQ: A Bayesian inference software framework for integration of data with complex predictive models under uncertainty *arXiv preprint arXiv:2112.00713*
- [30] Ambikasaran S and Darve E 2013 An $\mathcal{O}(n \log n)$ fast direct solver for partial hierarchically separable matrices *Journal of Scientific Computing* **57** 477–501
- [31] Ambikasaran S, O’Neil M and Singh K R 2014 Fast symmetric factorization of hierarchical matrices with applications *arXiv preprint arXiv:1405.0223*
- [32] Halko N, Martinsson P G and Tropp J A 2011 Finding structure with randomness: Probabilistic algorithms for constructing approximate matrix decompositions *SIAM Review* **53** 217–288
- [33] Xi Y, Xia J and Chan R 2014 A fast randomized eigensolver with structured LDL factorization update *SIAM Journal on Matrix Analysis and Applications* **35** 974–996
- [34] Boukaram W, Turkiyyah G and Keyes D 2019 Randomized GPU algorithms for the construction of hierarchical matrices from matrix-vector operations *SIAM Journal on Scientific Computing* **41** C339–C366
- [35] Gelfand I M and Fomin S 1963 *Calculus of variations* (Dover)
- [36] Cuffey K M and Paterson W S B 2010 *The physics of glaciers* (Academic Press)
- [37] Dukowicz J K, Price S F and Lipscomb W H 2010 Consistent approximations and boundary conditions for ice-sheet dynamics from a principle of least action *Journal of Glaciology* **56** 480–496
- [38] Larour E, Seroussi H, Morlighem M and Rignot E 2012 Continental scale, high order, high spatial resolution, ice sheet modeling using the Ice Sheet System Model (ISSM) *Journal of Geophysical Research: Earth Surface* **117**
- [39] Morlighem M, Rignot E, Seroussi H, Larour E, Ben Dhia H and Aubry D 2010 Spatial patterns of basal drag inferred using control methods from a full-Stokes and simpler models for Pine Island Glacier, West Antarctica *Geophysical Research Letters* **37** L14502
- [40] Perego M, Price S and Stadler G 2014 Optimal initial conditions for coupling ice sheet models to Earth system models *Journal of Geophysical Research: Earth Surface* **119** 1894–1917
- [41] Petra N, Zhu H, Stadler G, Hughes T J R and Ghattas O 2012 An inexact Gauss-Newton method for inversion of basal sliding and rheology parameters in a nonlinear Stokes ice sheet model *Journal of Glaciology* **58** 889–903
- [42] Glen J W 1955 The creep of polycrystalline ice *Proceedings of the Royal Society of London, Series A, Mathematical and Physical Sciences* **228** 519–538
- [43] Pattyn F, Perichon L, Aschwanden A, Breuer B, de Smedt B, Gagliardini O, Gudmundsson G H, Hindmarsh R C A, Hubbard A, Johnson J V, Kleiner T, Kononov Y, Martin C, Payne A J, Pollard D, Price S, Ruckamp M, Saito F, Soucek O, Sugiya ma S and Zwinger T 2008 Benchmark experiments for higher-order and full-Stokes ice sheet models (ISMIP-HOM) *The Cryosphere* **2** 95–108
- [44] Daon Y and Stadler G 2018 Mitigating the influence of boundary conditions on covariance operators derived from elliptic PDEs *Inverse Problems and Imaging* **12** 1083–1102
- [45] Lindgren F, Rue H and Lindström J 2011 An explicit link between Gaussian fields and Gaussian Markov random fields: the stochastic partial differential equation approach *Journal of the Royal Statistical Society: Series B (Statistical Methodology)* **73** 423–498
- [46] Hoffman M J, Perego M, Price S F, Lipscomb W H, Zhang T, Jacobsen D, Tezaur I, Salinger A G, Tuminaro R and Bertagna L 2018 MPAS-Albany land ice (MALI): a variable-resolution ice sheet model for Earth system modeling using Voronoi grids *Geoscientific Model Development* **11** 3747–3780
- [47] Tezaur I K, Perego M, Salinger A G, Tuminaro R S and Price S F 2015 Albany/FELIX: a parallel, scalable and robust, finite element, first-order Stokes approximation ice sheet solver built for

- advanced analysis *Geoscientific Model Development* **8** 1197–1220
- [48] Liegeois K, Perego M and Hartland T 2022 PyAlbany: A Python interface to the C++ multiphysics solver Albany *Journal of Computational and Applied Mathematics* 115037
- [49] Trilinos Project Team T 2020 *The Trilinos Project Website* URL <https://trilinos.github.io>
- [50] Joughin I, Smith B, Howat I and Scambos T 2015 MEaSUREs Greenland ice sheet velocity map from InSAR data, version 2 URL <https://nsidc.org/data/NSIDC-0478/versions/2>
- [51] Perego M 2022 Large-scale PDE-constrained optimization for ice sheet model initialization *SIAM News Online*
- [52] Hillebrand T R, Hoffman M J, Perego M, Price S F and Howat I M 2022 The contribution of Humboldt Glacier, North Greenland, to sea-level rise through 2100 constrained by recent observations of speedup and retreat *The Cryosphere Discussions* **2022** 1–33